



HAL
open science

Detection of undercover karst features by geophysics (ERT) Lascaux cave hill

Cecile Verdet, Colette Sirieix, Antoine Marache, Joëlle Riss, Jean-Christophe Portais

► **To cite this version:**

Cecile Verdet, Colette Sirieix, Antoine Marache, Joëlle Riss, Jean-Christophe Portais. Detection of undercover karst features by geophysics (ERT) Lascaux cave hill. *Geomorphology*, 2020, 360, pp.1-13. 10.1016/j.geomorph.2020.107177 . hal-03166947

HAL Id: hal-03166947

<https://hal.inrae.fr/hal-03166947>

Submitted on 20 May 2022

HAL is a multi-disciplinary open access archive for the deposit and dissemination of scientific research documents, whether they are published or not. The documents may come from teaching and research institutions in France or abroad, or from public or private research centers.

L'archive ouverte pluridisciplinaire **HAL**, est destinée au dépôt et à la diffusion de documents scientifiques de niveau recherche, publiés ou non, émanant des établissements d'enseignement et de recherche français ou étrangers, des laboratoires publics ou privés.



Distributed under a Creative Commons Attribution - NonCommercial 4.0 International License

1 Detection of undercover karst features by geophysics (ERT)

2 - Lascaux cave hill -

3 Verdet Cécile^{1*}, Sirieix Colette¹, Marache Antoine¹, Riss Joëlle¹, Jean-Christophe Portais²

4 * Corresponding author: cecile.verdet@u-bordeaux.fr

5 1 – University of Bordeaux, CNRS, Arts et Metiers Institute of Technology, Bordeaux INP, INRAE, I2M
6 Bordeaux, F-33400 Talence, France.

7 2 – Ministère de la culture, Direction Régionale des Affaires Culturelles Nouvelle-Aquitaine, 54, rue
8 Magendie, 33000 Bordeaux

9 Keywords: karstic morphology, ERT, Geophysics, Geostatistics model.

10 Abstract

11 The study of karst features under a detrital cover is difficult to obtain using punctual traditional tools.
12 This paper presents a 3D geostatistical modeling of ERT (Electrical Resistivity Tomography) data to
13 describe undercover karst features. A case study was carried out on the karstic site of the prehistoric
14 decorated Lascaux cave (France). Geophysical measurements were used to define the limit between
15 outcropping Coniacian or Santonian limestones (southwest) and clayey sands (northeast), with a main
16 orientation of N140°. A geometrical description of the scarp was also constructed; pinnacles and
17 notches were found under the clayey sand detrital formation. By combining 3D ERT with
18 geomorphological and geological observations, the geometry of the stratigraphic limit between the
19 Coniacian and Santonian limestone could be determined. This stratigraphic limit separates two
20 domains, one is a potential aquifer, and acts as a feeder for the intermittent spring at the cave
21 entrance, while the other is less permeable, resulting in a permeability contrast with the later rock
22 type. All these observations help define the geological cave environment and ensure better protection
23 for the paintings.

24 1. Introduction

25 In general, a karst landscape can be defined as resulting from the dissolution of carbonated rocks, such
26 as limestone and dolomites (Mangin, 1975; Bakalowicz, 1999). The Lascaux cave is developed within
27 the upper cretaceous limestone karst (France). It is a decorated cave that contains prehistoric paintings
28 believed to date back to the Magdalenian era (Aujoulat *et al.*, 1998). As a UNESCO world heritage site,
29 the cave has many conservation needs: one of them is a better understanding of the surrounding area
30 and especially of its karst. Therefore, this paper focus on the detection of undercover
31 geomorphological karstic features localized at the northeast of the cave, *i.e.* upstream of the Lascaux
32 cave (Xu *et al.*, 2017).

33 The complexity of the karst is well known and its high heterogeneity can be seen as a result of a triple
34 porosity at different scales (Király, 1975; Halihan *et al.*, 1999; Worthington, 1999; Vacher and Mylroie,
35 2002; Ford and Williams, 2007): (1) matrix porosity, (2) fracture and crack porosity and (3) conduit
36 porosity. The water flowing throughout these multiple porosities dissolves the rocks and finally forms
37 characteristic geomorphological features such as sinkholes, pinnacles, karren, karst valleys, and caves.
38 In some instances, these features are covered (or filled in the case of caves) with allochthonous or
39 autochthonous materials such as sand and clay. Assessing these undercover karst features is quite
40 challenging using only classical techniques like drilling, mainly because of the high variability of the
41 karst medium. In addition, concerning the Lascaux site, only non-destructive methods can be used near
42 the cave, so geophysical methods are suitable.

43 Currently, geophysical methods are widely used in large-scale investigations. To assess karst, a few
44 techniques have proved effective: (1) ground-penetrating radar (GPR) has been used in some cases
45 (Chalikakis *et al.*, 2011; Carrière *et al.*, 2013; Kaufmann and Deceuster, 2014) where the karst is not
46 covered, especially with clay that absorbs the GPR signal; (2) microgravimetry can give good results to
47 detect superficial empty and filled voids and to characterize karst heterogeneity (Solbakk *et al.*, 2018);

48 (3) seismic refraction tomography is also frequently used on karst because it can give information at
49 great depth with a high spatial resolution (Guérin *et al.*, 2009; Valois *et al.*, 2010, 2011); (4) finally,
50 electrical resistivity tomography (ERT) is now widely used to characterize karstic features; to date, most
51 of the karstic structures identified are sinkholes (Zhou *et al.*, 2000; Valois *et al.*, 2010; Billi *et al.*, 2016;
52 Cueto *et al.*, 2018), voids (Chávez *et al.*, 2018; Prins *et al.*, 2019), soil and bedrock interface (Bermejo
53 *et al.*, 2016; Cheng *et al.*, 2019b), and karstic aquifer geometry (Kaufmann and Deceuster, 2014; Sirieix
54 *et al.*, 2014; Carriere *et al.*, 2015; Xu *et al.*, 2015, 2017; Cheng *et al.*, 2019a). For the Lascaux case, ERT
55 methods have been shown to be effective (Xu *et al.*, 2015).

56 The principle of ERT methods is to inject an electrical current between two electrodes and to measure
57 the potential difference between two other electrodes, from which the apparent resistivity is
58 processed. Next, an inversion process gives an image of the electrical property of the sub-surface. The
59 image can then be interpreted as follows: resistivity depends on both the nature of the soil and on its
60 degree of water saturation (Archie, 1942). Therefore the more saturated the soil is, the lower the
61 resistivity, so are clay-rich soils. Most of the images are produced in 2D, thus the 3D heterogeneity of
62 the underground is not always well sampled. For this reason, 3D ERT tools are currently considered to
63 take account of the variability of the sub-soil.

64 There are three main ways to achieve 3D electrical resistivity models. First, by using what is called true
65 3D ERT, where both the acquisition and inversion are done in 3D. This method was applied by
66 Chambers *et al.* (2011) to characterize a landslide, again by Chambers *et al.* (2012) to detect a bedrock
67 under river terraces, and by Chávez *et al.* (2018) to detect a karstic void under a Mayan pyramid. True
68 3D ERT requires a long measuring time, and because it needs a very specific electrode geometrical
69 arrangement in the field, it is not always achievable due to harsh terrain conditions, e.g. presence of
70 dense vegetation. Second, the quasi-3D ERT method, where the data are acquired along 2D lines, then
71 collated and inverted into 3D data sets. This method was used by Kneisel *et al.* (2014) to detect the
72 depth of permafrost and its variability, with electrodes set up on a regular grid, and by Cheng *et al.*

73 (2019a) on karst on a large scale to detect the interface between weathered (or fractured) limestone
74 and the unweathered bedrock. Finally, the third method is a 3D geostatistical modeling of 2D acquired
75 and inverted ERT profile data. Geostatistical methods have been used on other resistivity data, like Riss
76 *et al.* (2011) who used geostatistical modeling on a large set of VES (Vertical Electrical Sounding) data
77 in order to model apparent resistivity that can be inverted as a classical 2D ERT. Other examples
78 include: (1) the study carried out by De Benedetto *et al.* (2012) who assessed the clay content in the
79 soil using GPR and electromagnetic induction data coupled with a geostatistical analysis;(2) Benoit *et*
80 *al.* (2019) used geostatistical methods to find a correlation between hydraulic conductivity and
81 geoelectrical data acquired with ERT and induce polarization (IP) in a riverbed. The 3D ERT
82 geostatistical modeling method has already been applied to the south of the Lascaux cave by Xu *et al.*
83 (2016), on a large scale. The authors revealed some interesting features, such as geological limits at a
84 low resolution. The present study will therefore focus on a higher resolution method using 3D ERT
85 geostatistical modeling to detect undercover karst heterogeneity and geological interfaces upstream
86 of the Lascaux cave. The upstream area of the cave is important to acknowledge, as the water present
87 within this area could reach the cave, depending on the spatial distribution of the heterogeneities, and
88 their size, connectivity and permeability (Xu *et al.*, 2017). Indeed, those characteristics control the
89 water flow transporting biological or chemical compounds that could affect the painted walls. In
90 addition, this water flow changes the internal climatic parameters, like temperature and humidity
91 (Lacanette *et al.*, 2009; Lacanette and Malaurent, 2014), challenging the cave ecosystem.

92 2. Study area

93 The study area is located in southwest France, in the Dordogne department, on the Lascaux hill,
94 upstream of the Lascaux cave (Figure 1.a). The entrance to the cave is located about 100 m above the
95 Vézère River. The karstic plateau that forms the hill consists of Coniacian and Santonian limestone. The
96 northeast of the study site is covered by clayey sands (Figure 1.a) whose origin is still debated, deriving

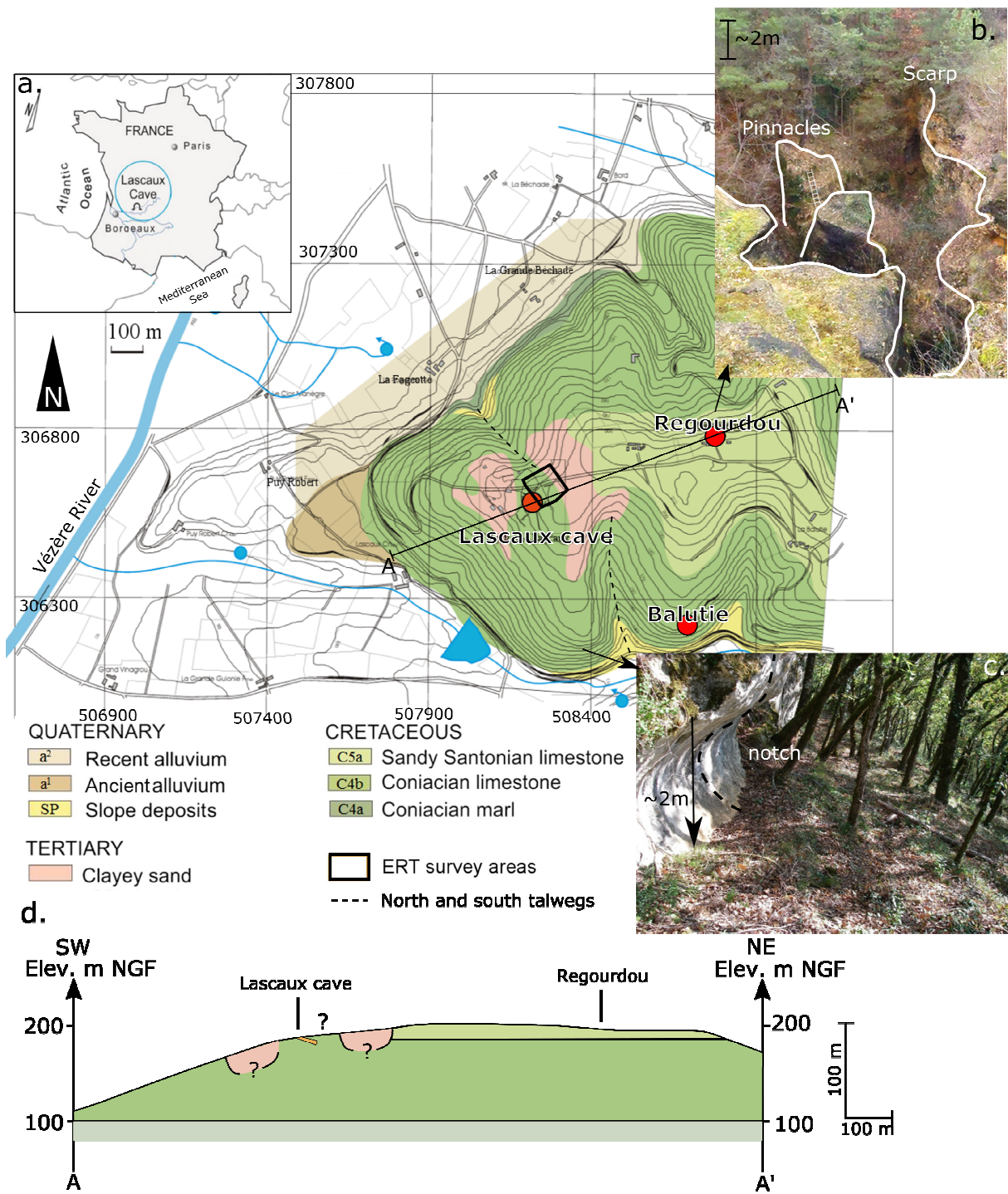
97 from autochthon alteration (Bruxelles and Camus, 2014; Xu *et al.*, 2017) or allochthon fillings of the
98 limestone (Lopez, 2009). Uncovered geomorphological features characterize the karst of the hill. The
99 naturally uncovered features are sinkholes (between the study site and the Regourdou site, Figure 2),
100 scarps (at the Regourdou site, Figure 1.b)) and a notch (Balutie archeological site and southeast of the
101 Lascaux cave, Figure 1.c). Other known karstic features on site are few caves: Lascaux cave, small caves
102 at the Balutie site and in the scarp southeast of the Lascaux cave. At the top of the hill, there is a site
103 called Regourdou where the clayey sand filling was removed manually, uncovering pinnacles, caves,
104 and scarps (Figure 1.b).

105 At a different scale, a map of the site shows that this study area covers middle and upper Coniacian
106 limestone and clayey sand filling to the northeast (Figure 2). The middle and upper Coniacian (C4b,
107 Figure 1.a) is characterized by a yellow bioclastic limestone and sandy limestone, with a presence of
108 hummocky cross-stratification (HCS) with a thickness of 50 to 70 m. The upper part is made of a
109 compact limestone, with an arenaceous part mixed with gravel and bioclastic debris (Guillot *et al.*,
110 1979). The Lascaux cave developed within this upper part. At the regional scale, the very top of the
111 Coniacian deposit is characterized by an oyster-rich level, 5 m thick (Platel, 1987), with a pale yellow
112 limestone formations (Guillot *et al.*, 1979; Platel, 1987). This level has never been described within the
113 Lascaux cave.

114 The top of the hill is constituted of Santonian limestone. The lower Santonian is characterized by a
115 chalky limestone that forms small plates, sandstone and yellow sands with a thickness between 40 and
116 60 m. The base level of the Santonian is formed of very small white-yellow chalky limestone with a
117 nodulous jointing aspect (Platel, 1987). Above, a lithological ensemble is formed of a red sandy
118 bioclastic limestone (30 to 60 m thick (Platel, 1987)). The Regourdou site is found within this part
119 (Guillot *et al.*, 1979).

120 The Lascaux cave seems to have developed along some of the directions that are recognized on the
121 hill: the structural map (Figure 2) displays four main fracture families (Lopez, 2009) with directions
122 running N178°E (F1), N119°E (F2), N93°E (F3) and N145°E (F4). These fracture directions are known at
123 the regional scale: direction F1 is close to the Larche fault direction, direction F2 is close to that of the
124 Condat and Cassagne faults, formed during the Hercynian orogenesis, and direction F3 is close to that
125 of the Meysac fault (Guillot *et al.*, 1979). The F3 and F1 families can be attributed to the tertiary
126 tectonic and the Pyrenean orogenesis (Guillot *et al.*, 1979). Another fracture direction, F1', is proposed
127 by Lopez (2009) that was not reported on the stereographic projection. Direction F4 is not found in the
128 other regional faults but is a known Hercynian direction in the region (Muller and Roger, 1977). The
129 directions of the two talwegs situated to the northwest and southeast of the cave are parallel to F4
130 and F1 respectively (Figure 1 and Figure 2). The main stratification plane above the Lascaux cave shows
131 a direction of N2°E with a dip of 4 to 6°SE (Lopez, 2009, Figure 2). Regarding the geomorphological
132 aspect, it should be noticed that the steepness of the hill slope becomes smoother at the top.

133 Currently, there are two main uncertainties, represented by the question marks in Figure 1d. First, the
134 thickness of the clayey sand fillings, which is mainly unknown because of the high variability of the
135 bedrock geometry. Second, the Santonian/Coniacian limit around the cave, the eastern clayey sand
136 filling masks the limit at the location where the slope steepness changes. As the climatic condition of
137 the cave depends on the water path upstream the cave, these two uncertainties will be studied and
138 discussed further in this paper.

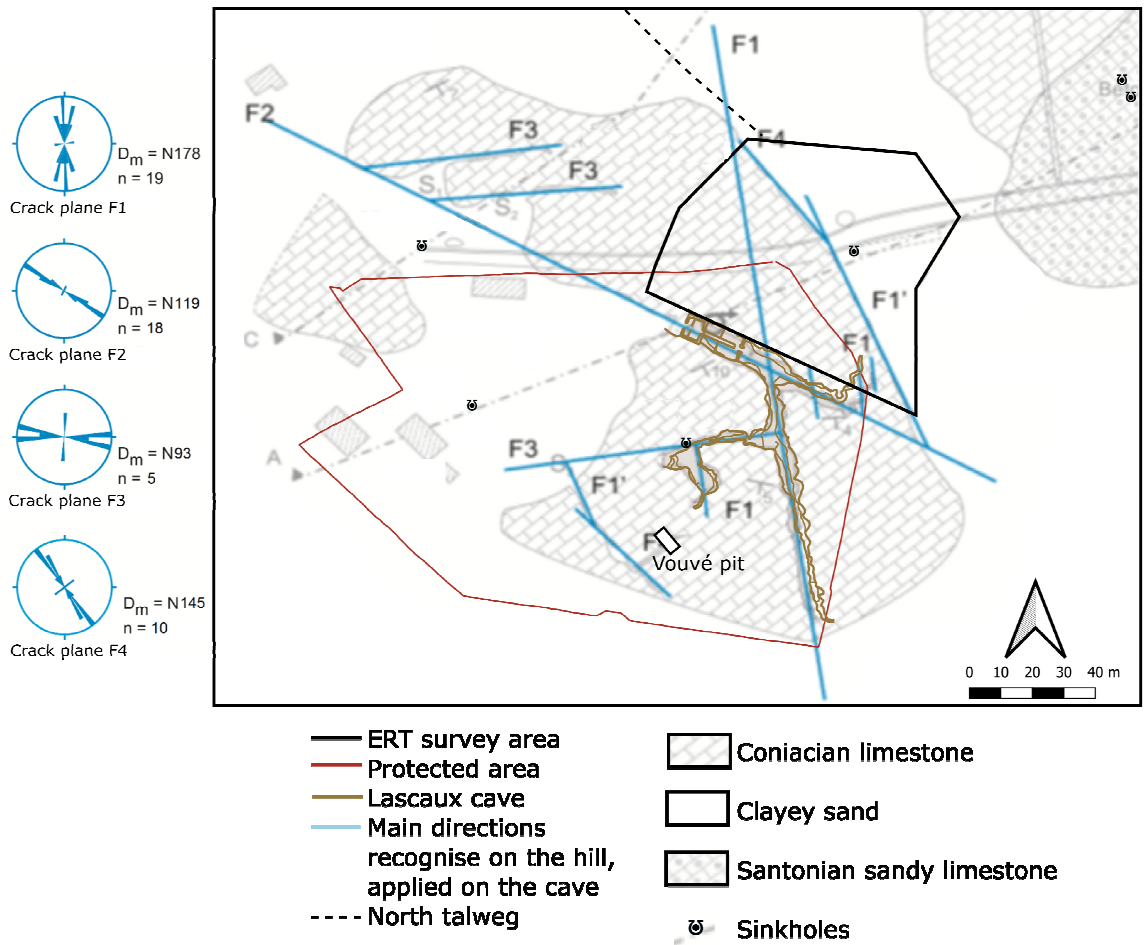


139

140 Figure 1: (a) Study area location with the geological map and site of interest (in Lopez (2009), Xu (2015) and Houillon (2016),

141 from Schoeller (1965)), (b) Regourdou scarp and pinnacles, (c) notch, (d) section along A-A' line. Note that the vertical scale is

142 twice the horizontal one. Question marks indicate the areas of uncertainty.



143

144 *Figure 2: Known sinkhole locations superimposed on the fracture report by Lopez (2009) on a map by Vouvé (1968). “n” is the*
 145 *number of fractures measured on site and “Dm” is the mean direction for each fracture family.*

146 **3. Methodology**

147 3.1. Electrical Resistivity Tomography

148 3.1.1. Survey design and inversion

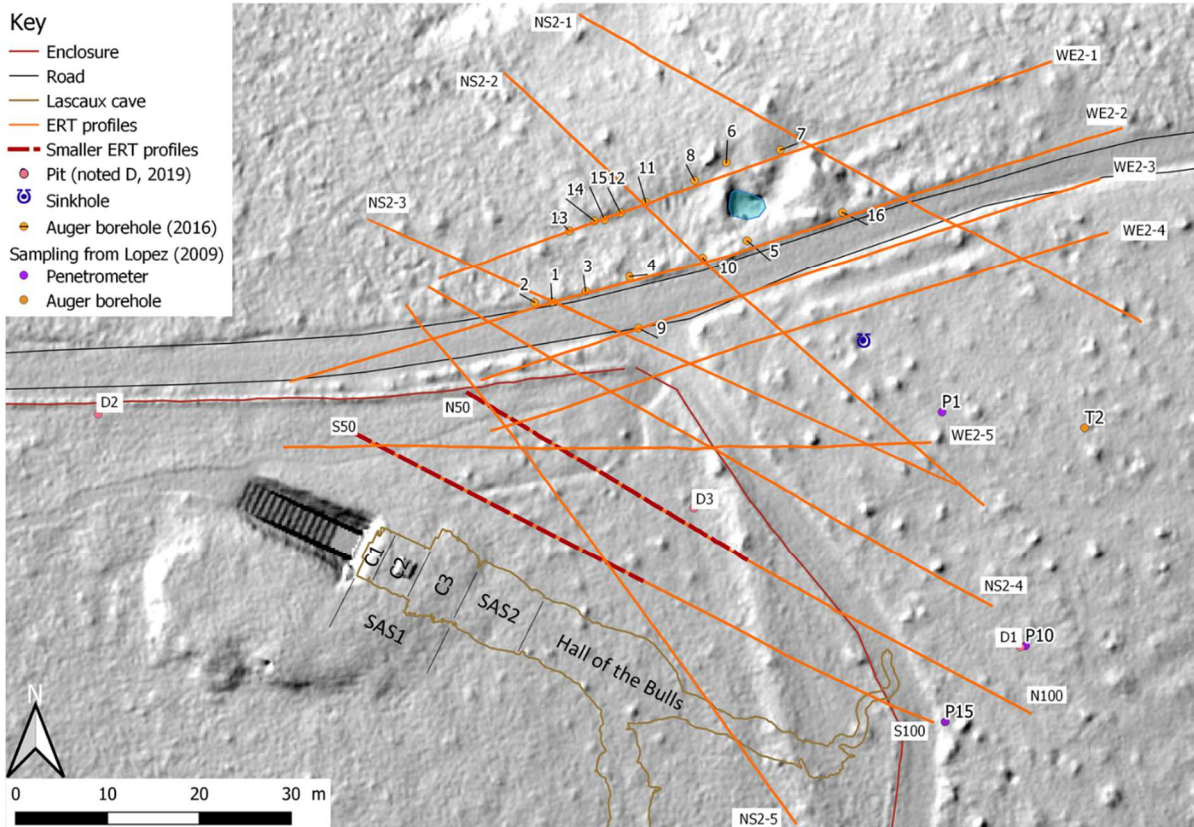
149 First of all, it should be noted that on site time-lapse monitoring indicated that the best season to carry
 150 out ERT measurement on the Lascaux epikarst is from January to July, as the soil is at its highest
 151 saturation point (Xu *et al.*, 2017). A high saturation will enhance the contrast between resistive and
 152 less resistive materials, making it interesting to target such a period for the ERT measurements. We
 153 therefore chose to do the survey in March 2018.

154 Secondly, the surveyed area is densely forested with many anthropic features. This was the main
155 constraint to the positioning of the ERT profiles and it conditioned the survey type. Because the true
156 3D process needs a precise electrode arrangement, usually a square with electrodes equally spaced on
157 a regular mesh, the use of a true 3D technique is not easily feasible on our site. Moreover, the presence
158 of anthropic features such as fences and buried electrical cables made 3D electrode implantation more
159 difficult. We therefore carried out a 2D survey designed to take into account the main known directions
160 on site, positioning the ERT lines perpendicularly to the directions. We also chose to produce a 3D
161 geostatistical model, since Xu *et al.* (2016) demonstrated that it gave good results on this site. Xu *et al.*
162 (2016) used a setup where the profiles were 20 m spaced among each other, with 96 electrodes spaced
163 at 1.5 m. The spacing between profiles is large, and, as we know, the karst heterogeneity is so variable
164 that information can be easily missed between the profiles. We reduced this spacing from 20 m in Xu
165 *et al.* (2016) to 5-10 m between two parallel profiles. As Sirieix *et al.* (2014) showed, the smaller the
166 electrode spacing, the better we can detect karstic features. Later, Xu *et al.* (2017) empirically
167 demonstrated that with a 1 m electrode spacing, features could be better defined on the Lascaux hill.

168 In order to improve the geostatistical model accuracy, it is interesting to acquire data in at least two
169 directions. The setup we chose is made up of 14 profiles (Figure 3). 11 profiles are made up of 72
170 electrodes spaced at 1 m, for a total length of 71 m (WE2-1, WE2-3, WE2-4, WE2-5; NS2-1, NS2-2, NS2-
171 NS2-3, NS2-4, NS2-5; N100, S100); 1 profile is made up of 96 electrodes spaced at 1 m, for a total length
172 of 95 m (WE2-2). Two profiles are refined near the cave, N50 and S50, made up of 72 electrodes spaced
173 at 0.5 m for a total length of 35.5 m. The spacing between profiles is about 5 to 10 m, covering an area
174 of about 5,500 m². The measurements were performed with an Iris Instrument Syscal Pro®. On each
175 profile, the current injection is carried out during 500 ms for pole-dipole and 250 ms for gradient
176 electrical array. The inversion is the result of a concatenation of three types of array: (1) a gradient ;
177 (2) forward and (3) reverse pole-dipole. The gradient array was selected because of its robustness, its
178 sensitivity to the vertical variations, its high spatial resolution and its velocity. The pole-dipole arrays

179 were used because of their velocity, their sensibility to voids and their good penetration depth. After
180 many tests, it appears that on the study site, the array that fitted best the depth of the compact
181 limestone is the concatenation of those two arrays (Xu, 2015). Data were filtered in order to remove
182 points with a quality factor above 5% (Peter-Borie *et al.*, 2011). As demonstrated by Xu *et al.* (2016),
183 the site anthropic noise is very low and can be found insignificant, the size of the electrode spacing is
184 adapted and a very small number of datum points were filtered. As a result, most of the profiles kept
185 their total number of datum points. On the worst-case scenario (profile WE2-4), only 9 datum points
186 out of 9,133 were removed. The inversion was performed with Res2DInv® software (Loke, 2004)
187 v. 4.05.38. with L1 norm as it is adapted on a heterogeneous medium with abrupt variability, which is
188 the case for the karst. The mesh was refined to half the electrode spacing. The absolute error of the
189 models was between 0.34% and 3.9%. After inversion, the total number of resistivity datum points was
190 32,845.

191



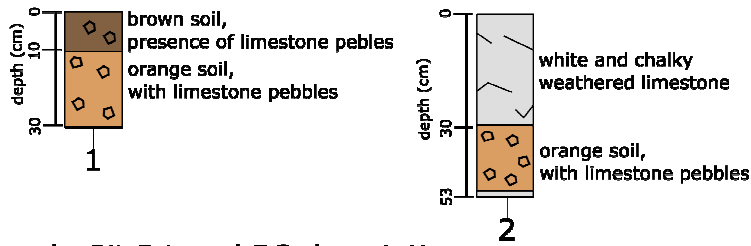
192

193 *Figure 3: ERT profiles, augers (numbered 1-16), penetrometers (labeled P1, P10, P15), and small pits (labeled D1-D3) location*
 194 *on a DEM (Digital Elevation Model) by Muth (2017). SAS1 is the first airlock, composed of three compartments C1, C2 and C3*
 195 *and SAS2 is the second airlock. No paintings are present in the two airlocks.*

196 The experimental one-off sampling plan comprised cone penetrometer test (CPT) data acquired by
 197 Lopez (2009) near the area of investigation (Figure 3). It was completed by superficial auger boreholes
 198 along the WE2-1 and WE2-2 profiles. These data (Figure 4) are to be used later in the paper to complete
 199 the interpretation of the 3D geostatistical model, alongside the other geomorphological observations
 200 made on the hill (see “study area” description). Also, two small pits were dug in July 2019, marked D1
 201 and D3 in Figure 3, and gave a direct view of the first 40 centimeters. Pit D1 was dug in the clayey sand
 202 area, D3 in the limestone area (Figure 1.a).

a. Auger boreholes, dug till refusal,

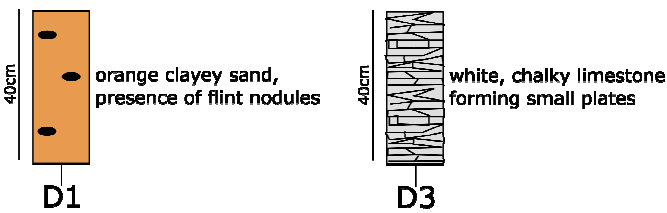
(i) Example with auger n°1 and 2



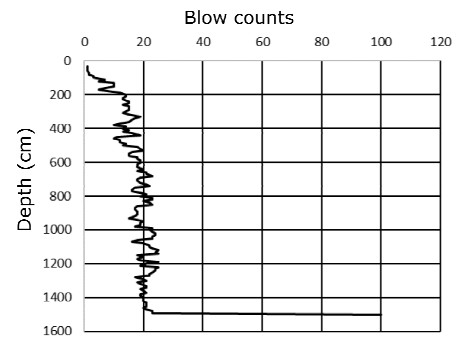
(ii) Synthesis of all other augers

| Augers in limestone | | Augers in clayey sand | |
|---------------------|------------|-----------------------|------------|
| n° | depth (cm) | n° | depth (cm) |
| 3 | 25cm | 16 | 360cm |
| 4 | 66cm | 6, 7 | 50cm |
| 13, 14 | 20cm | 11, 12, 15 | 25cm |

b. Pit D1 and D3 description



c. Penetrometer P1



204

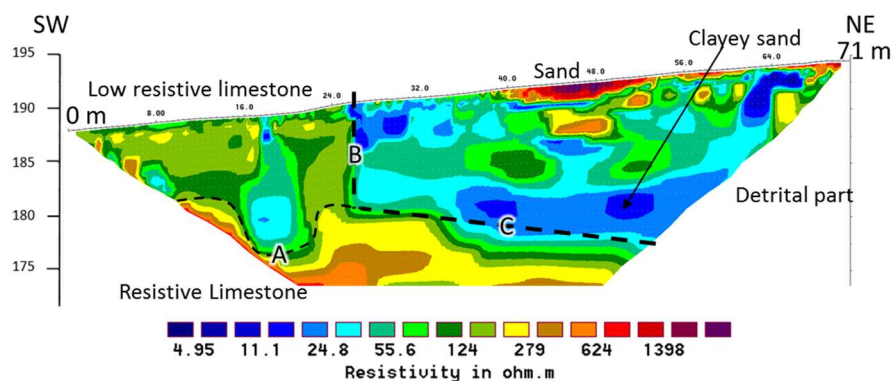
205 Figure 4: description of (a) auger boreholes with (a.i) augers n°1 and 2 in example, and (a.ii) synthesis of the refusal depth for
 206 augers showing limestone materials and depth investigated (not to the refusal) for augers showing clayey sand formation
 207 with flint nodules; (b) description of pits D1 and D3; (c) penetrometer P1 result, with a refusal depth at 15m.

208 3.1.2. 2D results

209 Each 2D electrical resistivity image displayed the same pattern of resistivity (Figure 5):

- 210 - In the northeast area of the profile (to the right of limits B and C), there is a part with a globally
- 211 low resistivity, and with a high inner variability. Field observations, augers and pit D1 (Figure
- 212 4.b) showed that this part is mainly formed of clayey sand. At the surface, some highly resistive
- 213 patches are present, which are the signature of clearer sand.
- 214 - In the southwest, at depth (below limits A and C) there is a globally high resistivity part with a
- 215 low variability. As Verdet *et al.* (2018) and Xu *et al.* (2016, 2015) showed, such resistivity is due
- 216 to the massive limestone bedrock. This is also supported by penetrometer P1 (Figure 4.c) data
- 217 that gave a refusal depth of 15 m (Figure 3).

218 - In the southwest, near the surface (to the left of limit B, above limit A), there is a mildly resistive
 219 part with an inner variability. Xu *et al.* (2017) indicated that this part is made up of different
 220 limestones from the previous one. They also indicated that this limestone has a resistivity that
 221 varies with time; therefore, its water content evolves. This superficial part was called
 222 weathered Coniacian limestone by Houillon (2016) and Xu *et al.* (2016), corresponding to the
 223 epikarst as defined by Mangin (1975).



224

225

Figure 5: WE2-4 profile with the geological interpretation reported.

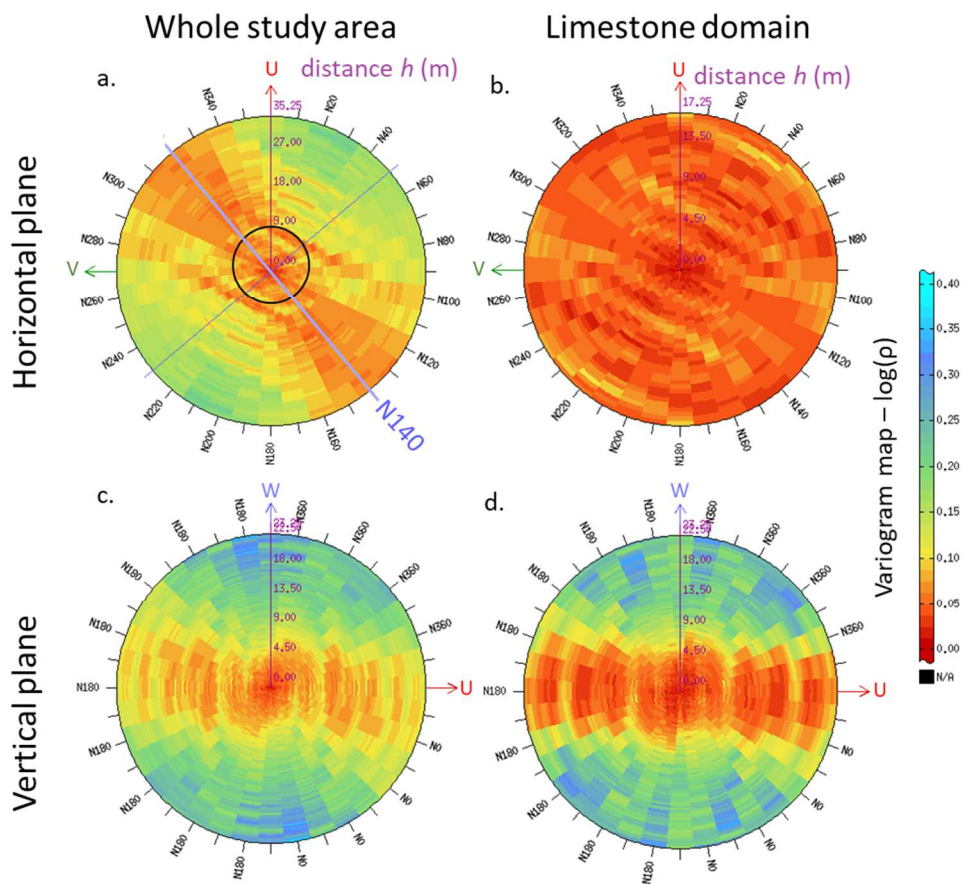
226 3.2. 3D geostatistical modelling

227 Several steps make up the geostatistical modeling process. The first is to statistically observe the raw
 228 inverted data. The mean resistivity is 164 $\Omega\cdot\text{m}$, varying from 3 to 5,119 $\Omega\cdot\text{m}$. In order to perform the
 229 variographic calculus, giving an understanding of the spatial structure of our data, and to avoid any
 230 influence from extreme values, we kept values between 10 and 1,000 $\Omega\cdot\text{m}$ (representing 98% of all
 231 values, *i.e.* 32,250 values). As these extreme values could have a physical significance, they are added
 232 for the final 3D kriging modeling process. The variogram study and the kriging model are made from
 233 the \log_{10} of the resistivity and are transformed into resistivity at the end for the final analysis.

234 The first tool we use is a variographic map (variomap), enabling us to observe the data structure in all
 235 directions. In particular, it makes anisotropy stand out (if anisotropy exists for the studied variable),
 236 and gives correlation length(s). The first map is computed using the ERT data from the whole study

237 area. On this map, two anisotropic directions are unveiled: one in the horizontal plane, with direction
 238 N140°, and one vertically (Figure 6.a and c). We can see that the variomap (Figure 6.a) remains isotropic
 239 under 10 m in the horizontal plane.

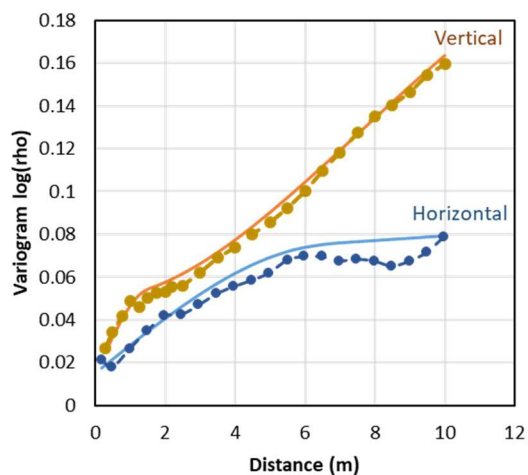
240 A second variomap is built using ERT data from the limestone part only, in the southwest of the study
 241 area. The N140° direction present on the whole site does not appear, nor does any other anisotropy
 242 direction in the horizontal plane (Figure 6.b). Only a vertical anisotropy appears (Figure 6.d), as the one
 243 found over the whole study area.



244
 245 Figure 6: Variographic maps for (a and c) the whole study area, and (b and d) the limestone area only. (a and b) represents
 246 the horizontal plane and (c and d) represents the vertical plane. \vec{U} , \vec{V} and \vec{W} are the three vectors giving the three main
 247 orientations of the 3D space. The color scale represents the $\log(\rho)$ variogram value.

248 The experimental variogram is then calculated in two directions: one in the horizontal plane and one
249 in the vertical plane. The experimental variogram in the horizontal plane is calculated isotopically as
250 the neighborhood will have a radius of 10 m for the kriging process (see below). The corresponding
251 theoretical variogram is then fitted on the experimental variogram as a combination of four
252 elementary models (Figure 7), providing that the lag stays under 10 m so the N140° anisotropy
253 direction can be ignored:

- 254 - A nugget effect with a sill at 0.015;
- 255 - A spherical model with a sill at 0.035, a range of 7 m in the horizontal plane and 1.5 m in the
256 vertical plane;
- 257 - A second spherical model with a sill at 0.018, a range of 6 m in the horizontal plane and 500 m
258 in the vertical plane;
- 259 - A cubic model with a sill of 0.19, a range of 500 m in the horizontal plane and 25 m in the
260 vertical plane.



261

262 *Figure 7: Experimental (dotted lines) and theoretical (continuous lines) variograms in both horizontal and vertical planes.*

263 In order to validate the variogram model, a cross-validation can be performed. The cross-validation is
264 a process that compares the true measured values to the values estimated by kriging at the same
265 points. The validation coefficient calculated with this method is 0.95, based on 32,250 experimental

266 data. Given this coefficient and this very large number of points, we consider that the variogram model
267 is validated.

268 After this variographical study, the next goal is to estimate a resistivity value at each node of a regular
269 grid by the kriging method. The chosen grid has an elemental cell size of 0.5m x 0.5m x 0.5m, because
270 of the size of the inversion grid used with the geophysical software. The kriging needs a defined
271 neighborhood to determine the volume around a grid node for which the resistivity value will be
272 estimated. The experimental points within this neighborhood will be used for the estimation at the
273 grid node. In our case, this neighborhood is a 10 m diameter sphere. The total number of estimated
274 points after kriging is 1,246,592.

275 Then the model is intercepted with the Digital Elevation Model (DEM, X. Muth, personal
276 communication) in order to remove estimated points above the topographical surface.

277 4. Results and discussion

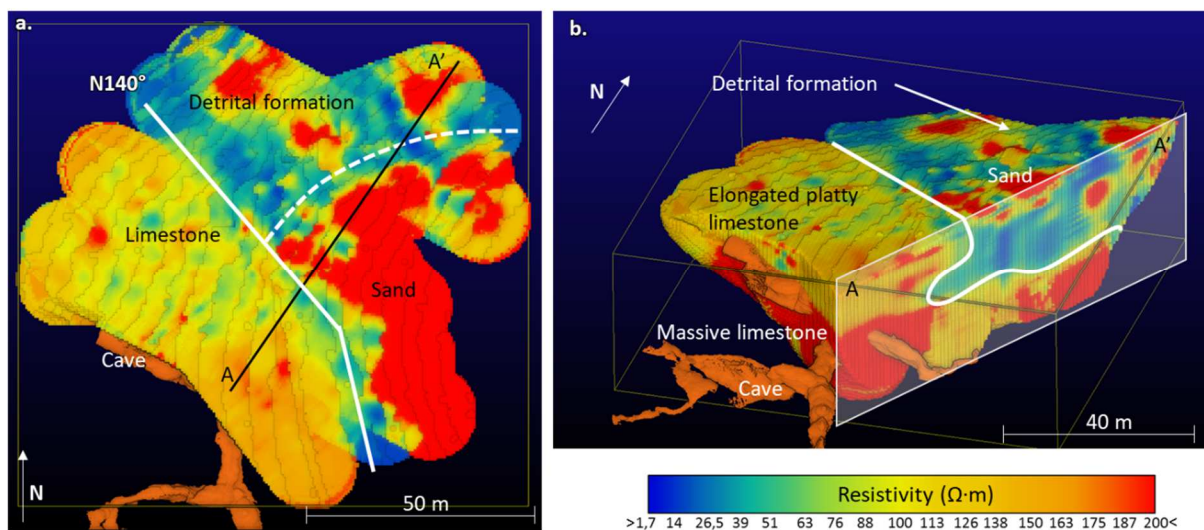
278 The 3D electrical model obtained is shown in Figure 8. Already, a few features stand out, such as the
279 N140° orientation. The geological limits are outlined later in this section ; so are the geomorphologic
280 karstic features under the cover of other detrital material.

281 4.1. Geological limit precision

282 First of all, the 3D resistivity model can be divided into two main domains, separated by the N140°
283 vertical limit already found with the variogram maps. The two domains can be interpreted with the
284 help of auger boreholes, penetrometer data, small pits (Figure 3 and Figure 4) and old pictures of the
285 cave entrance, before being widened (Figure 9). The N140° direction could correspond to the N145°
286 structural direction cited earlier. Looking at the structural map (Figure 2), the N145° (F4) direction
287 seems to separate the limestone part from the detrital part. Xu *et al.* (2016) also found a structural
288 direction of N145° by geostatistics, to the south and next to our study site, on the Lascaux hill.

289 Secondly, in the northeast, the first domain has a mainly low resistivity with a median of 68 $\Omega\cdot\text{m}$ (Figure
 290 8). In the southeast of the domain, a very superficial zone appears with a maximum thickness of 2 m
 291 and a very high median resistivity of 640 $\Omega\cdot\text{m}$. The low resistivity part is made up of detrital clayey-
 292 sand, found with augers 6, 7, 8, 11, 12, 15 and 16 (Figure 3). The high resistivity part is composed of
 293 sands that can be observed at the surface, directly on the floor and in pit D1 (Figure 3). These
 294 formations were also characterized in the southern part of the site by Xu *et al.* (2016) and Bruxelles
 295 and Camus (2014), Xu (2015).

296



297

298 *Figure 8: 3D resistivity model interpreted using auger and Vouvé boreholes. (a) View from above, with the superficial limits*
 299 *and the A-A' section position. (b.) View from the south, with a section along A-A' that shows the internal structure.*

300 In the southwest, the second domain has a globally higher resistivity, attributed to limestone, as it has
 301 been found in augers 1, 2, 3, 4, 5, 10, 13 and 14 (Figure 3). It can be separated into two subzones
 302 (Figure 8.b.):

- 303 - a superficial one, above 181 mNGF (French ordnance datum), heterogeneous with a median
 304 resistivity of 140 $\Omega\cdot\text{m}$. The entrance of the cave develops within this subzone;

305 - a deeper one, below 181 mNGF, and more homogeneous, with a higher median resistivity of
306 493 $\Omega\cdot\text{m}$. The Hall of the Bulls (Figure 3), one of the decorated chambers of Lascaux, as well as
307 the rest of the cave develops within this resistive subzone.

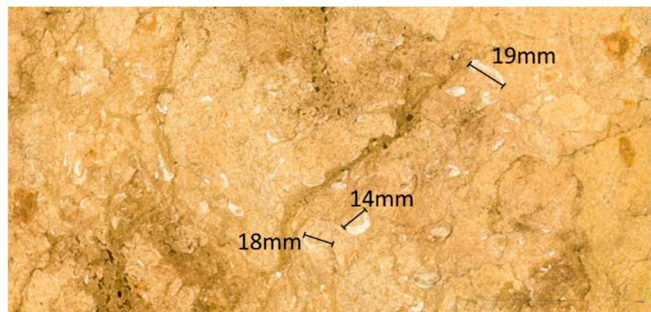
308 Xu *et al.* (2016) also identified these two domains at a wider scale and south of our study site, with a
309 median resistivity of 150 and 556 $\Omega\cdot\text{m}$ respectively, and an elevation of the limit of 179 mNGF. These
310 values are virtually the same, allowing for measurement accuracy. Auger reconnaissance (n°1, 2, 3, 4,
311 13, 14, Figure 4.a) and Vouvé boreholes (sampled from 1965 to 1968, described and published *in* Xu
312 (2015)) show that the whole zone is made up of limestone. The top part (above 181 mNGF) has a low,
313 variable resistivity, probably indicating a limestone with a globally high porosity and water or clay
314 content; while the lower part has a higher resistivity, thus more homogeneous, indicating a more
315 massive limestone. The limit between these two kinds of limestone found with the geophysical ERT
316 method is therefore between 181 mNGF \pm 1.5 m (this study) and 179 mNGF \pm 2 m (Xu *et al.*, 2016).
317 The uncertainty about the altitude is determined from the size of the inversion blocks at this depth.

318 We observe an outcrop on historical pictures of the site (Figure 9). At the top of Figure 9.a (above
319 approx. 185 mNGF) and in Figure 9.b, we can see a limestone made up of elongated small plates with
320 a filling in between the joints. Between 185 and 183 mNGF (Figure 9.a), the limestone is covered with
321 calcite, but seems to consist of the same elongated small plates. Such a limestone, which is easily
322 weathered, could perfectly explain the low resistivity of 140 $\Omega\cdot\text{m}$ found previously for the top part. The
323 top limestone can also be observed in the recent pit D3 (190 mNGF) as centimetric chalky, slightly red
324 and yellow, with elongated small plates, and a clayey-sand filling in the joints. In the south, an old pit
325 (Vouvé pit in Figure 2), dug in the 1960's and partially filled since, allows direct observation of the limit
326 between the two limestones (Figure 10). This clearly delineated boundary is estimated at around
327 182 mNGF in the Vouvé pit, in good agreement with a sedimentary origin well known in the literature
328 (Platel, 1987) rather than an erosion origin.



330

331 *Figure 9: Historic picture of the cave entrance before it was widened. (a) SAS1 C3 is now located here (see Figure 3). The limits*
 332 *of approx. 185.5 and 183 mNGF are estimated from the recent 3D model of the cave (picture Windels 1940-1941). (b) It is*
 333 *known that the feet of Laval are above 183mNGF, so the whole outcrop is above 183mNGF. The SAS1-C1 is now located here*
 334 *(picture Larivière 1940-09, Brive, from right to left: M. Breuil, Marsal (discoverer), Ravidat (discoverer) and Laval)). We can*
 335 *observe in the upper part that the limestone forms elongated small plates with a filling in between the joints.*



336 *Figure 10: Limit between elongated small plates and compact limestone observed in the Vouvé pit south of*
 337 *the cave (downstream). (Picture Verdet).*

336 *Figure 11: Detail of the oyster-rich level seen in the roof of the*
 337 *“Hall of the Bulls” (Picture Studio Guichard/Pérazio Engineering).*

336 The deeper part with a higher resistivity ($493 \Omega \cdot m$) is made up of a more compact limestone, as can be
 337 observed within the cave and on the historical photo in Figure 9.a, Figure 10 and Figure 11, below the

338 approximate 183 mNGF limit. It is mostly covered with calcite, and where visible, it forms multi-
339 decimetric slabs. We also observed an oyster-rich level in the roof of the “Hall of the Bulls”, at an
340 altitude of 181-182 mNGF (Figure 11), making it a part of the massive limestone. The oysters observed
341 measure about 1 to 2cm, so they could be *Ceratostreon pliciferum auricularis*. We have also found this
342 oyster-rich level in other parts of the cave, always between 178 mNGF and 182 mNGF. The geological
343 log for the Perigordian Region (Guillot *et al.*, 1979; Platel, 1987) shows that such an oyster-rich level is
344 the last stratigraphic level of the upper Coniacian stage, with no oysters found in the lower Santonian
345 limestone. So, the oyster-rich level observed in the cave defined the limit between Coniacian limestone
346 and the Santonian limestone on the site.

347 Besides the limit altitude of 182 mNGF defined by the oyster-rich level, the altitude is quite constant
348 across the whole site in the ERT model (this study, Xu *et al.* (2016)), with a very small dip, if any. The
349 N140° direction – or any other horizontal anisotropy direction – has not been found on the variographic
350 map computed on the limestone part (Figure 6.c), showing that the two kinds of limestone, each with
351 its own lithology, must be homogeneous – horizontally and at our scale – with a sub-horizontal dip.

352 Previously, other authors (Lopez, 2009; Houillon, 2016; Verdet *et al.*, 2016; Xu *et al.*, 2016, 2017) said
353 that the difference between the two parts (top with a resistivity of 140 $\Omega\cdot\text{m}$, and bottom with a
354 resistivity of 493 $\Omega\cdot\text{m}$) was due only to the difference in weathering effect. On the top was a limestone
355 identified as the epikarst, and below a limestone identified as the infiltration/transmission zone
356 (Houillon, 2016). In this present study, the dip of the limit between the two limestones is sub-horizontal
357 (close to the one found by Lopez (2009)) and the thickness of the top layer is not constant (thicker at
358 the top than at the bottom of the site, and the top layer of limestone was never found to the west of
359 the studied site). These observations are not consistent with the hypothesis of a difference in
360 weathering according to depth as the only explanation for this top layer.

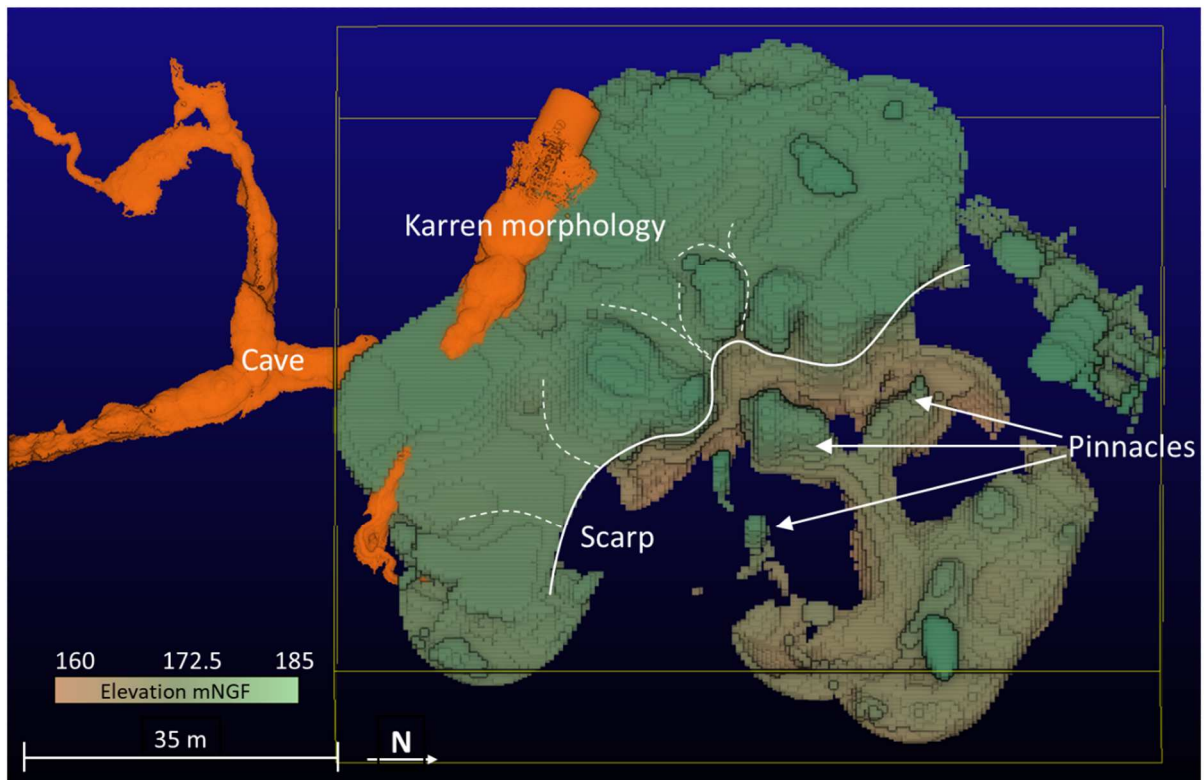
361 Moreover, the nature of the two kinds of limestone is not the same. Platel (Guillot *et al.*, 1979 and
362 Platel, 1987 completed with a personal communication, 2019) described the lower Santonian
363 limestone as isotropic and chalky, forming centimetric chips separated by marly beds. Platel (1987, and
364 personal communication, 2019) described the top of the upper Coniacian as a shelly limestone, rich in
365 oysters 2 to 3 cm in size, marking a visible limit with the Santonian limestone. Furthermore, on the
366 Guillot *et al.*, (1979) geological map, the geological limit clearly follows the topography around the hill,
367 forming a smoother plateau at the top. The limit is roughly at an altitude between 180 and 190 mNGF.
368 What we observe throughout this study is consistent with the Platel description. Therefore, we
369 conclude that the top part, with a low resistivity, is made up of Santonian limestone, whereas the
370 bottom part, with a higher resistivity, is made up of Coniacian limestone. Moreover, the Santonian
371 limestone constitution makes it prone to a higher alteration than the Coniacian, and it is highly
372 weathered on site. The elevation of the limit between these two kinds of limestone is determined from
373 the 3D model (this study, the Xu *et al.* (2016) study) and the field observations between 179 and
374 183 mNGF on the study site. The synthesis of all our observations allows us to estimate the altitude of
375 this limit at around 182 mNGF. From this point, the Coniacian/ Santonian limit on the geological map
376 is modified, as shown in Figure 13. This changes the Vouvé idea (chapter "Vouvé" in Leroi-Gourhan and
377 Allain (1979)) that described the permeable limit as a marly horizon as the origin of the waterflow in
378 the SAS1 C3. Originally, Schoeller (1965) described this horizon as a small layer, 30-40 cm thick, made
379 up of a high water content limestone. Recently, Houillon *et al.* (2017) described a contrast in
380 permeability –rather than a marly horizon– allowing the water to flow into the cave at the roof of SAS1
381 C3 (Figure 3). Our study confirms the Schoeller (1965) description; besides, we think the contrast in
382 permeability is due to the contact between the compact Coniacian limestone limit and the Santonian
383 limestone with the weathered Santonian limestone acting as a potential aquifer for the water flowing
384 at the intermittent spring at the cave entrance.

385 4.2. Karst geomorphological aspect

386 The analysis of the whole resistivity model showed there are two main resistivity groups. They are
387 delimited by an arbitrary limit, based on the resistivity histogram: one above 250 $\Omega\cdot\text{m}$ and the other
388 below 250 $\Omega\cdot\text{m}$. The materials left when keeping the resistivity of the blocks (from the 3D model) below
389 250 $\Omega\cdot\text{m}$ comprise mainly the detrital clayey-sand formations and the platy limestone (Santonian
390 limestone). We chose here to focus on the shape of the compact limestone that emerged when we
391 keep the blocks with resistivity higher than 250 $\Omega\cdot\text{m}$. The depth of the compact limestone under the
392 detrital formation is confirmed by penetrometer P1 (Figure 3) by Lopez (2009) showing a refusal depth
393 at the same depth, *i.e.* at 176 mNGF. Most of the decorated part of the cave is located under this limit,
394 and therefore develops within the massive Coniacian limestone.

395 The vertical limit between the limestone and the detrital domains becomes clear and stands as a scarp
396 with a few notch zones (Figure 12), as observed at the Regourdou site (Figure 1.b.), to the south of the
397 hill site (Figure 1.c.), and at the Balutie site. This is also supported by earlier on site work by Vouvé
398 (Chapter Vouvé *in* Leroi-Gourhan and Allain (1979)) that showed the limit between the two domains
399 must form a scarp. We can also observe that the Coniacian limestone roof forms what could be
400 interpreted as karren morphologies between the scarp and the cave, with the karren channels
401 highlighted with dotted lines.

402 At the bottom of the detrital domain, the limestone shape becomes clearer as well and defines what
403 can be assimilated as pinnacles (Figure 12). This interpretation is coherent with the observations made
404 at the Regourdou site (Figure 1.b.) where pinnacles are visible.

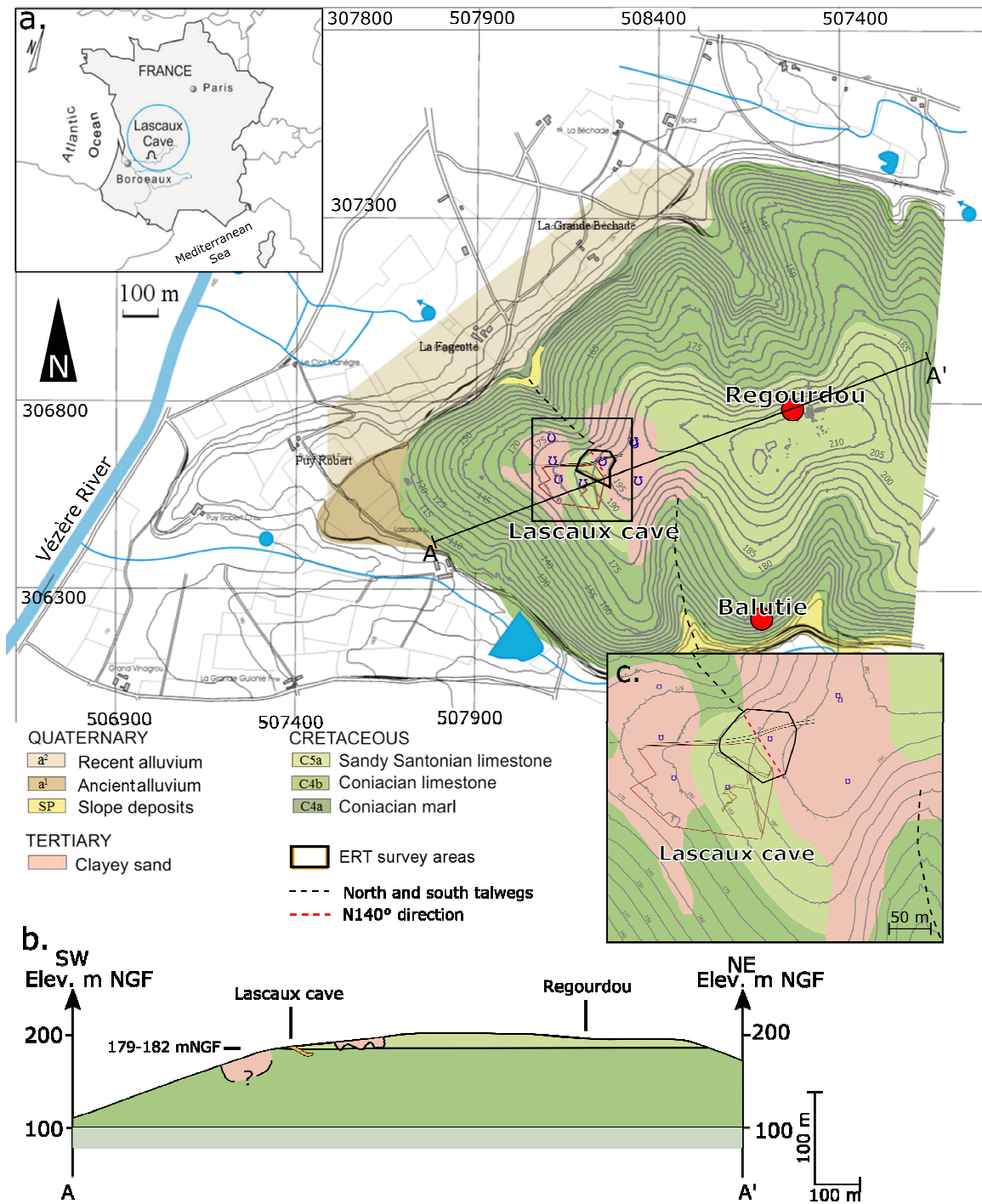


405

406 *Figure 12: View of the compact limestone. The plain arrows point to the pinnacles, the scarp is well defined. Karren morphology*
 407 *can also be observed (dotted lines) at the top of the limestone, north of the cave.*

408 The area upstream of the Lascaux cave shows a precise organization of its karstic features as described
 409 earlier in this paper, such as under-cover pinnacles, a notch and the limestone depth and geometry.

410 The geometry of the superficial limit of the limestone and clayey sand formation (Figure 8.a) can be
 411 reported at the scale of the hill (Figure 13.a). We observe that the northwest part of the limit has the
 412 same N140° orientation as the NW talweg (N137°) and prolongs it (Figure 13). We can assume that
 413 N140° is a fracture direction, which allowed the NW talweg to form (Figure 13). We can also assume
 414 that this fracture allowed the formation of a depression. Vouvé (chapter Vouvé *in* Leroi-Gourhan and
 415 Allain, 1979) showed there are two paleo-tributaries of the Vézère paleo-river present on the Lascaux
 416 hill, one at each side of the cave. We can assume that the south bank of the northern tributary could
 417 be the scarp that we found delimiting the limestone and the detrital clayey sand formation. The
 418 geological section is modified, as shown in Figure 13.b.



419

420 *Figure 13: (a) Modified geological map according to the findings of this present study. (b) Section along A-A' line. Note that*

421 *the Santonian limit and the depth of the NE sand filling are determined. The nature of the pinnacle is unknown, but could be*

422 *made up of Santonian. (c) Close-up of the study zone.*

423 5. Conclusion

424 The construction of a geostatistical 3D model based on ERT data provided a better understanding of
425 the Lascaux cave karstic environment geometry. The study area upstream of the cave shows two areas,
426 with a NW-SE limit separating limestones in the west from a clayey sand formation in the east. This
427 limit is an extension of the north talweg and is a structural direction. The high resolution of the 3D ERT
428 model uncovered unknown features of the site, such as pinnacles and a limit between the two kinds
429 of limestone. The limit between the upper Coniacian limestone and the lower Santonian limestone has
430 been redrawn thanks to geological and geomorphological observations on site along with the 3D ERT
431 model in order to match the 182 mNGF isohypse. We now assume that the entrance to the cave
432 develops within the small elongated chalky Santonian limestone plates; while the rest of the cave,
433 which is decorated, develops within the massive Coniacian limestone. Due to its constitution, the
434 Santonian limestone is more prone to weathering than the Coniacian, and therefore has a higher
435 permeability. It is likely a potential aquifer acting as a feeder for the intermittent spring at the cave
436 entrance. The water flowing through this intermittent spring can transport biological or chemical
437 compounds that could affect the painted walls, inducing potential conservation matters. In the
438 northeast of the site, the clayey sand formation lies above a limestone that forms undercover pinnacles
439 and a scarp.

440 Geological knowledge of the area around the cave is of great interest for its conservation. The limit
441 between the limestone and the detrital clayey sand formation to the northeast of the cave is well
442 known and could be used for protection purposes. The changes we have made to the Coniacian and
443 Santonian limit (more fractured, with clayey sand joint fillings and a higher water content) can be used
444 to adapt models of the cave environment, e.g. the thermal properties of the rocks around the cave or
445 the hydrogeological models applied to water circulation around the cave. Finally, the contrast in
446 permeability allows the presence of a perched aquifer, which feeds the spring at the entrance of the
447 cave. The permeability contrast is not due to a marly horizon; but to the contact between the lower

448 platy and permeable Santonian limestone and the upper compact shelly Coniacian limestone with a
449 lower permeability. It explains why the emergence in the cave entrance is located at this altitude and
450 at the limit between the Santonian and Coniacian limestones.

451 Acknowledgements

452 The authors would like to thank the French Ministry of Culture (DRAC Nouvelle-Aquitaine) for accessing
453 the cave surroundings and for their financial support. We especially thank Philippe Malaurent for his
454 help on the site and on the history of the site. He forms part of the memory of the Lascaux cave. We
455 also thank Fabien Naessens and Sylvain Mateo for their help with the field surveys (ERT and sampling).
456 We are very grateful to Jean-Pierre Platel for sharing his geological knowledge of the region and
457 Laurent Londeix for his help on the geology.

458 References

- 459 Archie, G.E., 1942. The electrical resistivity log as an aid in determining some reservoir characteristics,
460 in: *Transaction of American Institute of Mining, Metallurgical, and Petroleum Engineers*.
461 Dallas, pp. 54–62.
- 462 Aujoulat, N., Cleyet-Merle, J.-J., Gausson, J., Tisnerat, N., Valladas, H., 1998. Approche chronologique
463 de quelques sites ornés paléolithiques du Périgord par datation Carbone 14 en spectrométrie
464 de masse par accélérateur de leur mobilier archéologique. *Paléo* 319–323.
- 465 Bakalowicz, M., 1999. Connaissance et gestion des ressources en eaux souterraines dans les régions
466 karstiques. (Guide technique No. 3). Agence de l'eau Rhône-Méditerranée-Corse, Lyon.
- 467 Benoit, S., Ghysels, G., Gommers, K., Hermans, T., Nguyen, F., Huysmans, M., 2019. Characterization
468 of spatially variable riverbed hydraulic conductivity using electrical resistivity tomography and
469 induced polarization. *Hydrogeol. J.* 27, 395–407. <https://doi.org/10.1007/s10040-018-1862-7>
- 470 Bermejo, L., Ortega, A.I., Guérin, R., Benito-Calvo, A., Pérez-González, A., Parés, J.M., Aracil, E.,
471 Bermúdez de Castro, J.M., Carbonell, E., 2016. 2D and 3D ERT imaging for identifying karst
472 morphologies in the archaeological sites of Gran Dolina and Galería Complex (Sierra de
473 Atapuerca, Burgos, Spain). *Quat. Int.* 433, 393–401.
474 <https://doi.org/10.1016/j.quaint.2015.12.031>
- 475 Billi, A., De Filippis, L., Poncia, P.P., Sella, P., Faccenna, C., 2016. Hidden sinkholes and karst cavities in
476 the travertine plateau of a highly-populated geothermal seismic territory (Tivoli, central Italy).
477 *Geomorphology* 255, 63–80. <https://doi.org/10.1016/j.geomorph.2015.12.011>
- 478 Bruxelles, L., Camus, H., 2014. Grotte de Lascaux. Formes et formations anciennes de surface et sub-
479 surface. (rapport d'étude No. PRO-R-2014-03). Inrap, Protée et Ceneau, Montignac, Dordogne.
- 480 Carriere, S.D., Chalikakis, K., Danquigny, C., Clement, R., Emblanch, C., 2015. Feasibility and limits of
481 electrical resistivity tomography to monitor water infiltration through karst medium during a
482 rainy event, in: *Hydrogeological and Environmental Investigations in Karst Systems*. Springer,
483 pp. 45–55.

484 Carrière, S.D., Chalikakis, K., Sénéchal, G., Danquigny, C., Emblanch, C., 2013. Combining Electrical
485 Resistivity Tomography and Ground Penetrating Radar to study geological structuring of karst
486 Unsaturated Zone. *J. Appl. Geophys.* 94, 31–41.
487 <https://doi.org/10.1016/j.jappgeo.2013.03.014>

488 Chalikakis, K., Plagnes, V., Guerin, R., Valois, R., Bosch, F.P., 2011. Contribution of geophysical methods
489 to karst-system exploration: an overview. *Hydrogeol. J.* 19, 1169–1180.
490 <https://doi.org/10.1007/s10040-011-0746-x>

491 Chambers, J.E., Wilkinson, P.B., Kuras, O., Ford, J.R., Gunn, D.A., Meldrum, P.I., Pennington, C.V.L.,
492 Weller, A.L., Hobbs, P.R.N., Ogilvy, R.D., 2011. Three-dimensional geophysical anatomy of an
493 active landslide in Lias Group mudrocks, Cleveland Basin, UK. *Geomorphology* 125, 472–484.

494 Chambers, J.E., Wilkinson, P.B., Wardrop, D., Hameed, A., Hill, I., Jeffrey, C., Loke, M.H., Meldrum, P.I.,
495 Kuras, O., Cave, M., Gunn, D.A., 2012. Bedrock detection beneath river terrace deposits using
496 three-dimensional electrical resistivity tomography. *Geomorphology* 177–178, 17–25.
497 <https://doi.org/10.1016/j.geomorph.2012.03.034>

498 Chávez, R.E., Tejero-Andrade, A., Cifuentes, G., Argote-Espino, D.L., Hernández-Quintero, E., 2018.
499 Karst Detection Beneath the Pyramid of El Castillo, Chichen Itza, Mexico, by Non-Invasive ERT-
500 3D Methods. *Sci. Rep.* 8, 15391. <https://doi.org/10.1038/s41598-018-33888-9>

501 Cheng, Q., Chen, X., Tao, M., Binley, A., 2019a. Characterization of karst structures using quasi-3D
502 electrical resistivity tomography. *Environ. Earth Sci.* 78, 285. <https://doi.org/10.1007/s12665-019-8284-2>

503
504 Cheng, Q., Tao, M., Chen, X., Binley, A., 2019b. Evaluation of electrical resistivity tomography (ERT) for
505 mapping the soil–rock interface in karstic environments. *Environ. Earth Sci.* 15.

506 Cueto, M., Olona, J., Fernández-Viejo, G., Pando, L., López-Fernández, C., 2018. Karst-induced sinkhole
507 detection using an integrated geophysical survey: a case study along the Riyadh Metro Line 3
508 (Saudi Arabia). *Surf. Geophys.* 12.

509 De Benedetto, D., Castrignano, A., Sollitto, D., Modugno, F., Buttafuoco, G., Papa, G. Io, 2012.
510 Integrating geophysical and geostatistical techniques to map the spatial variation of clay.
511 *Geoderma* 171–172, 53–63. <https://doi.org/10.1016/j.geoderma.2011.05.005>

512 Ford, D., Williams, P.W., 2007. Karst hydrogeology and geomorphology, Rev. ed. ed. John Wiley & Sons,
513 Chichester, England ; a Hoboken, NJ.

514 Guérin, R., Baltassat, J.-M., Boucher, M., Chalikakis, K., Galibert, P.-Y., Girard, J.-F., Plagnes, V., Valois,
515 R., 2009. Geophysical characterisation of karstic networks – Application to the Ouyse system
516 (Poumeyssen, France). *Comptes Rendus Geosci.* 341, 810–817.
517 <https://doi.org/10.1016/j.crte.2009.08.005>

518 Guillot, P.-L., Feys, R., Lefavrais-Raymond, A., Platel, J.-P., Lefavrais-Henry, M., 1979. Notice de la carte
519 géologique de la France à 1/50 000 - Terrasson (n°784).

520 Halihan, T., Sharp Jr, J.M., Mace, R.E., 1999. Interpreting flow using permeability at multiple scales.
521 *Karst Model. Karst Waters Inst. Spec. Publ.* 5, 82–96.

522 Houillon, N., 2016. La dynamique du carbone inorganique dans le continuum sol-épikarst-cavité du site
523 de la Grotte de Lascaux (Dordogne, France): apports des monitorings hydrogéochimique et
524 microclimatique continus pour l'étude de l'aérogologie et le développement d'une méthode de
525 simulation des processus calco-carboniques aux parois (Thèse). Université de Bordeaux.

526 Houillon, N., Lastennet, R., Denis, A., Malaurent, P., Minvielle, S., Peyraube, N., 2017. Assessing cave
527 internal aerology in understanding carbon dioxide (CO₂) dynamics: implications on calcite
528 mass variation on the wall of Lascaux Cave (France). *Environ. Earth Sci.* 76.
529 <https://doi.org/10.1007/s12665-017-6498-8>

530 Kaufmann, O., Deceuster, J., 2014. Detection and mapping of ghost-rock features in the Tournais area
531 through geophysical methods—an overview. *Geol. Belg.* 17, 17–26.

532 Király, L., 1975. Rapport sur l'état actuel des connaissances dans le domaine des caractères physiques
533 des roches karstiques. *Hydrogeol. Karstic Terrains Hydrogéologie Terrains Karstiques Int.*
534 *Union Geol. Sci.* 53–67.

535 Kneisel, C., Emmert, A., Kästl, J., 2014. Application of 3D electrical resistivity imaging for mapping
536 frozen ground conditions exemplified by three case studies. *Geomorphology* 210, 71–82.
537 <https://doi.org/10.1016/j.geomorph.2013.12.022>

538 Lacanette, D., Malaurent, P., 2014. Préviation climatique 3D dans la grotte de Lascaux. *Karstologia* 49–
539 57.

540 Lacanette, D., Vincent, S., Sarthou, A., Malaurent, P., Caltagirone, J.-P., 2009. An Eulerian/Lagrangian
541 method for the numerical simulation of incompressible convection flows interacting with
542 complex obstacles: Application to the natural convection in the Lascaux cave. *Int. J. Heat Mass*
543 *Transf.* 52, 2528–2542. <https://doi.org/10.1016/j.ijheatmasstransfer.2008.12.028>

544 Leroi-Gourhan, A., Allain, J., 1979. *Lascaux inconnu*. CNRS.

545 Loke, M.H., 2004. Tutorial : 2-D and 3-D electrical imaging surveys.

546 Lopez, B., 2009. *Les processus de transfert d'eau et de dioxyde de carbone dans l'épikarst* (Thèse).
547 University of Bordeaux.

548 Mangin, A., 1975. *Apport de l'hydrodynamique pour la compréhension des aquifères karstiques*
549 (Thèse). Université de Dijon.

550 Muller, J., Roger, P., 1977. L'Evolution structurale des Pyrénées (Domaine central et occidental). Le
551 segment hercynien, la chaîne de fond alpine. *Géologie Alp.* 149–191.

552 Muth, X., 2017. DEM of the Lascaux hill.

553 Peter-Borie, M., Sirieix, C., Naudet, V., Riss, J., 2011. Electrical resistivity monitoring with buried
554 electrodes and cables: noise estimation with repeatability tests. *Surf. Geophys.* 9, 369–380.
555 <https://doi.org/10.3997/1873-0604.2011013>

556 Platel, J.-P., 1987. *Le créacé supérieur de la plate-forme septentrionale de Bassin d'Aquitaine.*
557 *stratigraphie et évolution géodynamique.* (Thèse). Université Bordeaux III.

558 Prins, C., Thuro, K., Krautblatter, M., Schulz, R., 2019. Testing the effectiveness of an inverse Wenner-
559 Schlumberger array for geoelectrical karst void reconnaissance, on the Swabian Alb high plain,
560 new line Wendlingen–Ulm, southwestern Germany. *Eng. Geol.* 249, 71–76.
561 <https://doi.org/10.1016/j.enggeo.2018.12.014>

562 Riss, J., Luis Fernández-Martínez, J., Sirieix, C., Harmouzi, O., Marache, A., Essahlaoui, A., 2011. A
563 methodology for converting traditional vertical electrical soundings into 2D resistivity models:
564 Application to the Saïss basin, Morocco. *GEOPHYSICS* 76, B225–B236.
565 <https://doi.org/10.1190/geo2010-0080.1>

566 Schoeller, H., 1965. Étude géologique, hydrogéologique et climatologique de la grotte de Lascaux
567 pendant le cycle 1964-1965. *Rapp. Détude* 30.

568 Sirieix, C., Riss, J., Rey, F., Prétou, F., Lastennet, R., 2014. Electrical resistivity tomography to
569 characterize a karstic Vauclusian spring: Fontaine d'Orbe (Pyrénées, France). *Hydrogeol. J.* 22,
570 911–924. <https://doi.org/10.1007/s10040-013-1095-8>

571 Solbakk, T., Fichler, C., Wheeler, W., Lauritzen, S.-E., Ringrose, P., 2018. Detecting multiscale karst
572 features including hidden caves using microgravimetry in a Caledonian nappe setting: Mefjell
573 massif, Norway. *Nor. J. Geol.* <https://doi.org/10.17850/njg98-3-04>

574 Vacher, H.L., Mylroie, J.E., 2002. Eogenetic karst from the perspective of an equivalent porous medium.
575 *Carbonates Evaporites* 17, 182.

576 Valois, R., Bermejo, L., Guérin, R., Hinguant, S., Pigeaud, R., Rodet, J., 2010. Karstic morphologies
577 identified with geophysics around Saulges caves (Mayenne, France). *Archaeol. Prospect.* 17,
578 151–160. <https://doi.org/10.1002/arp.385>

579 Valois, R., Camerlynck, C., Dhemaied, A., Guerin, R., Hovhannissian, G., Plagnes, V., Rejiba, F., Robain,
580 H., 2011. Assessment of doline geometry using geophysics on the Quercy plateau karst (South

581 France): morphology of dolines using geophysics. *Earth Surf. Process. Landf.* 36, 1183–1192.
582 <https://doi.org/10.1002/esp.2144>

583 Verdet, C., Sirieix, C., Riss, J., 2018. Détermination du fonctionnement hydrogéologique d'un site
584 karstique par un suivi temporel en tomographie de résistivité électrique – Epikarst de la grotte
585 de Lascaux, in: *Actes Du 11ème Colloque de Géophysique Des Sols et Des Formations*
586 *Superficielles*. Presented at the 11e Colloque GEOFCAN, Anthony, pp. 81–84.

587 Verdet, C., Xu, S., Sirieix, C., Riss, J., Allègre, V., 2016. Cluster analysis of time-lapse resistivity data to
588 identify a privileged feed zone within the epikarst of Lascaux Cave (France). Presented at the
589 43rd IAH International Congress: "Groundwater and society: 60 years of IAH," Montpellier, p.
590 127.

591 Vouvé, J., 1968. Travaux préliminaires dans le cadre de l'aménagement d'un nouvel accès dans la
592 grotte de Lascaux - Creusement d'un puits. Ministère des Affaires Culturelles, Périgueux.

593 Worthington, S.R., 1999. A comprehensive strategy for understanding flow in carbonate aquifers. *Karst*
594 *Model*. Eds Palmer MV Palmer ID Sasowsky Spec. Publ. 30–37.

595 Xu, S., 2015. Caractérisation de l'environnement karstique de la grotte de Lascaux par couplage de
596 méthodes géophysique, statistique et géostatistique (Thèse). Université de Bordeaux.

597 Xu, S., Sirieix, C., Ferrier, C., Lacanette-Puyo, D., Riss, J., Malaurent, P., 2015. A geophysical tool for the
598 conservation of a decorated cave – a case study for the Lascaux cave. *Archaeol. Prospect.* 22,
599 283–292. <https://doi.org/10.1002/arp.1513>

600 Xu, S., Sirieix, C., Marache, A., Riss, J., Malaurent, P., 2016. 3D geostatistical modeling of Lascaux hill
601 from ERT data. *Eng. Geol.* 213, 169–178. <https://doi.org/10.1016/j.enggeo.2016.09.009>

602 Xu, S., Sirieix, C., Riss, J., Malaurent, P., 2017. A clustering approach applied to Time-Lapse ERT
603 interpretation - case study of Lascaux Cave. *J. Appl. Geophys.*
604 <https://doi.org/10.1016/j.jappgeo.2017.07.006>

605 Zhou, W., Beck, B.F., Stephenson, J.B., 2000. Reliability of dipole-dipole electrical resistivity
606 tomography for defining depth to bedrock in covered karst terranes. *Environ. Geol.* 39, 760–
607 766.
608